Modeling Studies on the Formation of Hurricane Helene: The Impact of GPS Dropwindsondes from the NAMMA 2006 Field Campaign

Michael J. Folmer

ESSIC, University of Maryland

Robert W. Pasken *

Saint Louis University

Sen Chiao

San Jose State University

Jason Dunion

NOAA AOML-HRD

Jeffrey Halverson

University of Maryland-Baltimore County

Submitted to Meteorology and Atmospheric Physics

August 25, 2015

1st Revision: December 2, 2015; 2nd Revision: February 2, 2016; 3rd Revision: March 20, 2016

* *Corresponding author address and current affiliation:* Dr. Robert Pasken, Department of Earth and Atmospheric Sciences, Saint Louis University, 3507 LaClede Ave., Saint Louis, MO 63103

E-mail: rpasken@slu.edu

ABSTRACT

Numerical simulations, using the Weather Research and Forecasting (WRF) model in concert with GPS dropwindsondes released during the NASA African Monsoon Multidisciplinary Analyses (NAMMA) 2006 Field Campaign, were conducted to provide additional insight on SAL-TC interaction. Using NCEP Final analysis (FNL) datasets to initialize the WRF, a sensitivity test was performed on the assimilated (i.e., observation nudging) GPS dropwindsondes to understand the effects of individual variables (i.e., moisture, temperature, and winds) on the simulation and determine the extent of improvement when compared to available observations. The results suggested that GPS dropwindsonde temperature data provided the most significant difference in the simulated storm organization, storm strength, and synoptic environment, but all of the variables assimilated at the same time give a more representative mesoscale and synoptic picture.

1. Introduction

Each hurricane season, about 50-60 tropical low-pressure disturbances exit the West Africa coast and propagate westward across the Atlantic. Approximately one-fifth of these disturbances become tropical depressions, tropical storms, or hurricanes. The ability to isolate which of these disturbances will or will not develop has presented a significant challenge through the years. The solution to this problem may lie in the understanding of the intricate interaction among Saharan dust storms (i.e. the Saharan Air layer or SAL), the West African Monsoon (WAM), and these tropical disturbances. The WAM is a seasonal reversal of the winds that provide beneficial rainfall to the Sahel, a region bounded by the Sahara Desert to the north and tropical rain forests to the south. The WAM originates when the mean wind out of the east or northeast is replaced by southwesterly winds at the surface which transport moist air from the tropical Atlantic over the Sahel, leading to heavy rains falling close to the southern edge of the Sahara. During the monsoon, the contrast between the hot Saharan air and relatively cooler air to the south gives rise to the African Easterly Jet (AEJ). Disturbances within the AEJ are commonly known as African Easterly Waves (AEWs). Approximately half of the hurricanes that impact the United States have origins as AEWs.

The National Aeronautics and Space Administration (NASA) conducted the NASA African Monsoon Multidisciplinary Analyses (NAMMA) field campaign from the Cape Verde Islands and western North Africa from August to September 2006. Major goals of the project were to: (1) identify and characterize AEWs and mesoscale convective systems (MCSs) over West Africa as they transition from land-based to ocean-based convective systems; (2) examine the formation and evolution of hurricanes from AEWs in the eastern and central Atlantic and their impact on the U.S. east coast; and (3) determine the composition and structure of the Saharan Air Layer (SAL), and whether aerosols affect cloud precipitation and influence tropical cyclone (TC) development. To carry out this investigation, NASA deployed surface observation networks and an aircraft to sample AEWs and MCSs as they moved from the

continental environment to the maritime environment. NASA also used its extensive array of orbiting satellites such as Aqua, TRMM, and Cloudsat/CALIPSO along with modeling to support the main objectives of the NAMMA field campaign. NASA's DC-8 medium altitude research aircraft served as the primary research tool for the NAMMA investigations, flying a compliment of 40 crew members and a variety of remote and in situ sampling sensors to measure aerosol, cloud, and meteorological parameters.

The data collected during the NAMMA DC-8 flights has provided significant insight into the role that the SAL plays in regulating tropical cyclogenesis. Dunion and Velden (2004) suggested that the SAL might suppress TC activity in the North Atlantic and documented its suppressing characteristics for a number of specific TC-SAL interactions that have occurred during several recent Atlantic hurricane seasons. Carlson and Prospero (1972) proposed that a dry, well-mixed layer often extends to roughly 500 hPa over Africa during the summer months. As this air mass advances westward from the North Africa coast, often in association with AEWs (Burpee 1972), it is undercut by cool, moist, low-level maritime air and becomes the SAL. Just offshore, the SAL's base is at roughly 900-1800 m and the top is usually below 5500 m (Diaz et al 1976). Near its southern boundary, the SAL is also associated with the mid-level AEJ centered near 700 hPa, which can greatly increase vertical wind shear (e.g., Dunion and Velden 2004). The SAL appears to retain its Saharan characteristics of warm, stable air near its base, and dryness and dustiness throughout its depth as it is carried as far as the western Caribbean Sea (approximately 7000 km from the West Africa coast).

Though it can promote convection along its western and southern boundary (Chen 1985), the SAL can act to suppress convection by enhancing evaporatively driven downdrafts which can disrupt any attempts at organization for a developing or well-developed TC (Emanuel 1989; Powell 1990). Dunion and Velden (2004) hypothesized that AEWs simply propagate into the SAL, while the low- to mid-level inflow of TCs advect the SAL's dry, dusty air into the TC circulation. This dry air is also associated with reduced values of convective available potential energy (CAPE), a measure of the stability of the atmosphere (Dunion

2011). Smaller values of CAPE imply greater atmospheric stability and therefore, reduced convective activity. SAL-targeted GPS sondes indicate that the SAL appeared to maintain its thermodynamic characteristics as it moved approximately 5000 km across the North Atlantic to a position less than 500 km off the southeast U.S. coast (Carlson and Prospero 1972). Dunion and Velden (2004) noted that the 29 SAL profiles they collected suggest that the variability of the moisture in the SAL is relatively low. The standard deviation of the 700 hPa relative humidity (RH) was less than eight percent for these soundings. These results are similar to the mean SAL atmospheric sounding that was later presented by Dunion (2011).

Much emphasis has been placed on the dry air and vertical wind shear associated with the SAL as contributors to the degeneration of many AEWs, but little has been done to decipher the exact impact. Braun (2010) has focused on the synoptic pattern as a possible reason for the degeneration of certain AEWs, suggesting that drying from synoptic-scale subsidence on the ridge side of the ITCZ circulation gets entrained into an AEW, leading to competing downdrafts that disrupt the low-level circulation. Another area that deserves some investigation is the role of the aerosols within the SAL as a contributor of competing cloud condensation nuclei (e.g., Centeno and Chiao 2015). Although the data collected during the NAMMA field campaign provides a detailed picture of the structure of both AEWs and MCSs, these data do not provide a description of the environment that the AEWs and MCS exist in and how that environment changes over time. By using the dropsonde data and a mesoscale model a detailed analysis of how AEWs interact with their environment can be constructed and how that interaction determines whether an AEW turns into a tropical depression, tropical storm, or hurricane. This detailed analysis could then be used to test hypotheses of how the SAL affects AEWs' in association with tropical depressions, tropical storms, or hurricanes, The goal of this study is to create this analysis and to test how sensitive the analysis is to the availability of data.

Section 2 describes the case and numerical experimental design, section 3 provides discussions of WRF simulation results, and section 4 offers conclusions.

2. Methodology

a. Description of the Case Study

Seven AEWs were sampled during the NAMMA 2006 Field Campaign near the Cape Verde Islands in the eastern North Atlantic. Figure 1 shows these AEWs, of which two developed rapidly (AEW 2 and AEW 7). The remaining AEWs either dissipated or were linked to TC development farther downstream in the western North Atlantic. The time period of our study was between AEW 6 and AEW 7. These AEWs were chosen based on the quality of the GPS dropwindsonde data and the contrast in their evolution as AEW 6 remained weak and dissipated, while AEW 7 eventually strengthened into a category 3 hurricane. Zawislak and Zipser (2010) noted that the 925 hPa vorticity associated with AEW 6 was very inconsistent (Fig. 1a), but a 700 hPa vorticity maxima tracked in concert with the 700 hPa wave trough through much of its lifecycle (Fig. 1b). Since AEW 6 did not develop into a tropical depression (Fig. 2a), the main focus of this paper was on AEW 7.

AEW 7, which became Hurricane Helene, had its origins in far eastern Africa in the vicinity of the Ethiopian Highlands. According to Zawislak and Zipser (2010), the vorticity maxima and AEW trough tracks in the Global Data Assimilation System (GDAS) analyses for this system were the longest and most consistent of any of the NAMMA AEWs. The northern track low-level and southern track mid-level vorticity maxima merged shortly after moving off the western Africa coastline on 11 September 2006 (Fig. 2b). A surface low quickly formed and was upgraded to the 8th tropical depression of the 2006 Atlantic season at 1200 UTC on 12 September. It strengthened to a tropical storm at 0000 UTC on 14 September and was upgraded to a hurricane at 1200 UTC on 16 September, which is beyond the scope of this study. Helene reached peak intensity as a 105 kt (54 ms^{-1}) category 3 hurricane at 0000 UTC on 18 September.

b. *Description of the Domain*

To accurately capture the transition of AEWs from West Africa to the Atlantic, the domain had to be large enough to account for the synoptic and geographic influences such as the AEJ and the Sahara Desert, respectively. Figure 3 gives a visual representation of the three domains used in this study, using a Lambert Conformal map projection. The horizontal grid spacing for the first domain is 36 km that spans from $4^o - 24^o$N and $2^o - 30^o$W. This places the west coast of Africa in the center of the domain and was done to ensure the AEW stays near the center of the domain for the duration of the simulation, while also allowing an adequate amount of the dry air associated with the SAL to be simulated correctly as it interacts with the AEW/TC. The first nested domain is a 12 km grid ($8^o - 19^o$N, $9^o - 27^o$W), which focuses on the synoptic scale interaction with the AEW/TC in a more mesoscale environment. The West African coastline is in the eastern third of this domain to capture the transition from continental to maritime environments, while the Cape Verde Islands are located in the northwest corner of the domain. The final nested domain is a 4 km grid ($10.5^o - 16^o$N, $14^o - 26^o$W). This inner domain focuses attention on the vortex at 700 hPa and eventually the surface circulation once the system moved to south-southeast of the Cape Verde Islands. The finer resolution of this domain also provides more detail when simulating the behavior of convection near the vortex as well as the intricate interactions in the boundary layer.

The AEW transitions from a continental convective regime to a maritime tropical regime, with dry, dusty air and cool sea surface temperatures (SSTs) along the immediate coastline possibly playing a significant role. It has been noted that this region is a source region for long-tracked, Cape Verde hurricanes. A Cape Verde hurricane is defined as any TC that develops within 600 nautical miles of the Cape Verde Islands. Using that definition, a quick climatology of this domain was conducted and revealed that approximately 76 systems developed in this region from 1851 to 2010. Although many Cape Verde systems have recurved around the western periphery of the subtropical ridge, passing harmlessly between

the United States and Bermuda, very few systems directly impacted the Cape Verde Islands. For instance, Hurricane Erin (1989) tracked directly through the islands as a tropical depression and Hurricane Felix (1989) formed to the northeast of the islands in what is typically a heavily dust-laden region. These two cases in particular would be considered anomalous as there most likely was less SAL in the region in 1989.

c. Sensitivity Tests

There has been significant interest in the role that the dry air and aerosols play in this evolution and whether it is the loading of aerosols or a combination of the aerosols, dry air, and vertical wind shear that make up the SAL. Another aspect to investigate is the direct or indirect contribution to TC degeneration or intensification. Sun et al. (2009) found that "the SAL warm temperatures may be the indirect but root cause or fundamental factor, whereas the dry air is a direct factor in leading to the TC suppression by increasing parcel stability in the vicinity of the developing storm." The authors suggested that the WRF could not adequately represent the near-storm environment as the dry air gets much closer to the circulation center than the model could simulate. Therefore, it is necessary to find the best possible simulation to most accurately depict the hostile synoptic and mesoscale environment in the Eastern Atlantic using non-forecast initialization and available dropwindsondes.

For the simulations of AEW 7, multiple sensitivity tests were conducted on the three domains previously described using the National Center for Atmospheric Research's (NCAR) Weather Research and Forecasting (WRF) model V3.1.1 to determine the optimal physics parameters and model initializations. The Global Forecast System (GFS) Final Analysis (FNL) dataset was used to initialize the model runs due to their data assimilation of available observations into a re-analysis as opposed to a model forecast. This approach was chosen to allow assimilated observations within the GFS FNL dataset to correct the WRF towards the real-time environment that was sampled during NAMMA 2006. The physics parameters chosen for these simulations are based on previous sensitivity studies using the WRF in

simulating Hurricane Helene in the eastern North Atlantic (Folmer 2009). The following physics parameters were used including: Thompson microphysics scheme (Hong et al. 2006), the Mellor-Yamada-Janjic TKE Scheme (Janjic 2001), the RUC land-surface model, the Goddard scheme for the shortwave radiation physics (based on Chou and Suarez 1994), Rapid Radiative Transfer Model (RRTM) scheme for the longwave radiation physics (Mlawer et al. 1997), and the Grell-Devenyi ensemble cumulus scheme. The control case simulation began on 09 September at 0000 UTC and continued to 14 September 2006 at 0000 UTC. The discussions in this study are based on the 12 km nest results.

With an adequate control case, the next step was to assimilate GPS dropwindsonde data that was collected on 09 September 2006 (AEW 6) and 12 September 2006 (AEW 7) as part of the NAMMA 2006 field campaign. These GPS dropwindsondes were launched from the NASA DC-8 from pressure altitudes ranging from 300-600 hPa. The locations of the dropsonde with overlaid MODIS satellite imagery are presented in Figure 4. Sondes dropped on September 9, 2006 are marked in green (Fig. 4a) and those dropped on September 12, 2006 are in red (Fig. 4b). Since the goal of the NAMMA field campaign was to determine whether aerosols in the Saharan Air Layer affect cloud precipitation and influence cyclone development these launch points were designed to sample the environment that the waves 6 and wave 7 were developing in. The GPS dropwindsonde data shows the near real-time environment both preceding and during the evolution of each AEW near or just southwest of the Cape Verde Islands. It was assumed that the GPS dropwindsondes would be a valuable asset to the data assimilation of the GFS FNL initialized WRF simulations. In a study by Wu et al. (2007), it was found that the track error reduction in the WRF was 16% when GPS dropwindsondes and initial conditions from the operational GFS were used. Nevertheless, the impacts from the GPS dropwindsondes assimilated with FNL data was unclear. The purpose of assimilating the GPS dropwindsondes in this study is to evaluate the quality and accuracy of the simulations involving AEW 7. The simulations included 15 GPS dropwindsondes (seven from 09 Sept 2006 and eight from 12 Sept 2006) and were then

compared to the control runs to isolate any systematic differences. The vertical resolution was set using the prescribed eta-levels of 27 for the GFS FNL dataset. The GPS dropsondes was utilized at these pre-determined levels.

It is worth noting that the NAMMA dropsonde data was quality controlled by the quality control procedures developed by NCAR. The NCAR dropsonde system has a long history of providing quality vertical atmospheric profiles from dropsondes. The dropsonde system has been in use for tropical cyclone and hurricane research for several decades (e.g., Tuleya and Lord 1997). A description of the accuracy of dropsonde measurements is documented in Hock and Franklin (1999) and a description of NCARs quality control procedures applied to a multiyear tropical cyclone dropsonde data can be found in Wang et al. (2015).

The dropsonde data was assimilated into the WRF using observation nudging rather than 3DVAR due to the lack of an appropriate background error covariance matrix. Although there is generic background error covariance matrix it is a global value and is not limited to the area around Cape Verde. Using a global value for a specific location may or may not produce improvements. Further the limited number of dropsondes launched during the field campaign, the changing location and the fact that no forecasts were available make computing observational error statistics and background covariance matrixes problematic. Observation nudging uses a weighted average of differences from observations within a radius of influence and time window. The horizontal radius of influence is chosen based on the density of observations and grid spacing. The vertical weighting is a chosen to be small value so that only observations at sigma levels only assimilated. The period over which an observation can have an influence is limited to a time window around the observation time and the influence is ramped up and then down over a selectable amount time within the window that the observation exerts an influence. For this study horizontal radii of influence were 240km, 80km and 26km, which is approximately 6 times the grid spacing for domains 1, 2 and 3 with a vertical weighting of 0.005 sigma level. The time window of 40 minutes was smoothly ramped up and the down associated with the nudging. Winds, temperature and

moisture observations from the dropsondes were used in the observation nudging process.

3. Model Results

a. Control experiments

Before assimilating the dropwindsondes into the WRF, an initial simulation was produced using only the GFS FNL initialization dataset as a control run. The control run resulted in an AEW that propagated westward and quickly intensified into a 976 hPa hurricane at 1200 UTC on 13 Sept 2006, near the southernmost Cape Verde Islands. By assimilating the GPS dropwindsonde data using observation nudging, the system only gradually intensified to 1006 hPa and remained somewhat more disorganized (very similar to observations). Figure 5 shows the Meteosat-8 infrared satellite imagery of AEW 7 at 1400 UTC on 12 Sept 2006. There was evidence of banding in the northwest quadrant, in juxtaposition with the SAL, with some weaker banding evident in the southeastern and northeastern quadrants. Figure 6a shows the outgoing longwave radiation (OLR) for the GFS FNL initialized simulation with no observation nudging. It is quite apparent that the system is more organized than the IR satellite image in Fig. 5 as the appearance is more symmetric, yet the same strong convection on the western flank is suggested with decent banding in all quadrants. The difference here is that the simulation shows an intensity of 994 hPa at this time, while the NHC Best track reports an intensity of 1007 hPa, two hours prior to this image. When all 15 GPS dropwindsondes were assimilated into the WRF (Fig. 6b), the intensity of the low associated with the AEW is decreased to 1002 hPa, much closer to the NHC Best track data. The AEW also looked more disorganized in this simulation with a lack of significant banding features, except for a weak band in the southwest quadrant and abundant dry air evident in the northern quadrant as evidenced by the higher OLR signature.

b. Sensitivity experiments

A series of sensitivity tests were performed to determine whether the temperature, relative humidity, or wind from the assimilated dropwindsondes contributed the most to the differences in and around the environment of AEW 7 and its evolution in association with SAL. Table 1 summarized all numerical experiments conducted in this study. The first numerical experiment (i.e., wGPS) assimilated only the wind measurements from the 15 GPS dropwindsondes with no additional thermodynamic or pressure data. At 1200 UTC 13 Sept 2006, the AEW had developed into a tropical depression according to the NHC Best track dataset and it was sufficiently far enough away from the coast of Africa to not to be disrupted by topographical influences. Figure 7 shows the difference in 600 hPa RH between the simulation with no four-dimensional data assimilation (FDDA) (i.e., **nGPS**) and the simulation with only the wind contribution from the GPS dropwindsondes (i.e., **wGPS**). The black ellipse isolates an area, as shown in Fig. 7, that is recurring in these sensitivity tests where nGPS experiment has RH on the order of 35%-40% higher than wGPS experiment. Considering there is no RH input from the GPS dropwindsondes, this signature could be a product of the strength of moisture advection in that band. This indicates that the wind from the GPS dropwindsondes was better to depict more dry air advection in the northern and eastern quadrants of AEW 7 than the GFS FNL data alone could provide. The cooler colors in Fig. 7 indicate areas where the wGPS experiment had higher RH than nGPS, but the most significant departures were near the low center and the arcing spiral band to the north. The inner core region of AEW 7 is generally drier when the GPS dropwindsondes winds were added.

A difference in the temperature field at 700 hPa was noted between nGPS and wGPS. It was likely due to a difference in low placement. As shown in Fig. 8, the difference is most notable near the TC center (black circle) where nGPS is 6°C warmer than wGPS. However, it appears as though the track of the 700 hPa low in wGPS is slightly faster and south of the low in nGPS. This leads to a -7°C cool spot slightly southwest of the warm

spot. Meanwhile, the difference in sea level pressure (SLP) is depicted in Figure 9 where the black circle denotes the location of the TC centers for each of the two simulations. The cool colors indicate a difference in SLP of about 26 hPa, which is not truly representative of the SLP differences between the two runs. At this time, nGPS had a central pressure of 976 hPa, while wGPS was at 987 hPa for a difference of 11 hPa. Much of the pressure difference is due to an offset of the TC center between the two simulations, but there is a notable difference in mean sea-level pressure (MSLP) at this time. This does indicate that the wind observations from the GPS dropwindsondes alone weaken the simulated TC. Difference plots of wind components (not shown) reveal some minor differences, but are misrepresented by the difference in the location of the TC center in the simulation. It is plausible that the reason for the slightly faster and farther south TC track is due to it being slightly weaker, therefore begin advected by the more easterly low to mid-level trade wind flow. The greatest impact of the wind from the GPS dropwindsondes was likely the advection of the lower RH air into and around the system, which led to a slightly weaker system, though still biased too strong.

The 2nd experiment was focused on the temperature component of the GPS dropwindsondes (i.e., tGPS), while the wind and RH were not included. The same fields were compared following the methods performed for the wind test, starting with the RH field at 600 hPa. Figure 10 shows the same RH band that appears in the wind test in the black ellipse, but this time nGPS has RH that is 15%-20% higher. There were notable differences in the western and southern quadrants where tGPS appears to be drier. The reasons for this are a bit unclear, but could be due to the difference in temperatures between the two runs. Since RH relies heavily on ambient temperature, higher temperatures lead to lower RH values as the column can hold more moisture, while the opposite is true for this case where tGPS is cooler in the TC environment than nGPS. Therefore, the effects of the drier air can be seen at work by the lower RH values when compared with Figure 7. Meanwhile, the temperature field in Figure 11 shows once again that the core of the TC in the nGPS experiment is warmer

than the core in tGPS (black circle) by 5^oC. The ring of cool colors may be a product of the cooling effects of downdrafts or precipitation processes within the model around a much more organized eyewall structure in nGPS. The overall presentation of the temperature field indicates that the nGPS experiment may be too warm in the storm environment as the addition of the temperature from the GPS dropwindsondes had a cooling effect of up to 2^oC within the TC's larger scale circulation. The significant band of cooling to the right of the black circle indicates a stronger band of convection in nGPS.

An analysis of the SLP difference field in Figure 12 reveals that both TC cores in the simulations followed a similar path as there is a lack of a couplet caused by position offsets. The nGPS experiment had a central pressure of 976 hPa, while tGPS had a central pressure of 991 hPa. This 15 hPa difference in SLP along with the differences noted in the other two fields suggest that the temperature component of the GPS dropwindsondes is quite significant as the GFS FNL dataset most likely does not have adequate temperature information to accurately represent this area. It is worth noting that the temperature departures put more weight on the SAL environment introducing a more stable environment in the northern and western quadrant of the TC circulation, thus limiting the convective activity in those quadrants, despite moist low-levels and warm SSTs ($> 26^oC$).

The 3rd sensitivity experiment was conducted using the GPS dropwindsonde RH (i.e., rGPS), while the temperature and wind were excluded from the assimilations. Figure 13 shows the band of relatively higher RH (40-50%) that was consistent with the other sensitivity tests. In fact, the nGPS RH was higher in an arcing band that extended into the southwest inflow channel of the TC. The lower RH in the rGPS simulation would likely negate rapid strengthening as convection would be initially intensified, but would eventually lead to many competing downdrafts that would act to disrupt the low to mid-level vortex.

In Figure 14, the temperature difference at 700 hPa is plotted and once again a distinct couplet is evident near the TC center. This is due to a slightly farther south location of the TC center in the rGPS experiment. The general circulation of nGPS was warmer than

rGPS, but cooler temperatures were noted on the fringes in most quadrants (except for the southern quadrant). This means that the temperatures at this level are warmer in the GPS dropwindsonde run, possibly due to the lower RH values from the assimilated GPS dropwindsondes. The difference in SLP is not presented though again, nGPS had a pressure of 976 hPa and rGPS has a pressure of 982 hPa. Although the addition of RH data from the GPS dropwindsondes did impact where moisture and temperature gradients existed in rGPS, it was not enough to significantly weaken the simulated TC.

When all three of the GPS dropwindsonde observation components (RH, temperature, and winds) are turned on in the assimilation (i.e., aGPS) , the TC takes on a much different form than that observed in nGPS. Using the same methods as the individual tests to compare differences, Figure 15 shows the most distinct band of higher RH in nGPS compared to aGPS. Values within the black ellipse are 50% higher in the simulation with no GPS dropwindsonde data. Lower RH values are also noted near the TC center, which suggests higher RH values in the GPS dropwindsonde data than the initialization data had. The temperature difference in Figure 16 is indicative of a much warmer mid-level core in nGPS and a much warmer peripheral TC circulation in aGPS (e.g., particularly in the northern semicircle), which could be evidence of the presence of the SAL. Finally, the SLP difference plot (Figure 17) shows a stark difference in pressure between the two simulations. By assimilating all of the thermodynamic and kinematic components of the GPS dropwindsondes into the model, the TC remains much weaker with a central pressure in aGPS of 1005 hPa, 29 hPa higher than in the nGPS simulation.

Another effective way to gauge the model performance in depicting the mesoscale environment is to compare the GPS dropwindsonde data with model analyses using collocated skew-T plots. The intent is for the simulation to represent the eastern North Atlantic synoptic and mesoscale environments as precisely as possible, rather than improving individual forecasts. Figure 18a shows the first GPS dropwindsonde released from the DC-8 on 09 Sept 2006 at approximately 1400 UTC (25.4^{o}W and 14.2^{o}N). The GPS dropwindsonde was

released from a flight level of approximately 500 hPa and therefore a full sample of the troposphere was not observed; the SAL area of interest is between 550 hPa and 950 hPa. Fairly dry air is noted between 950 hPa and 680 hPa, with a spike of very dry air around 650 hPa. This may reflect the GPS dropwindsonde responding from the change in aircraft environment to the airmass, but that is hard to decipher from here. Nevertheless, smaller values of CAPE imply greater atmospheric stability and therefore, reduced convective activity. A skew-T plot from the same coordinates in the control GFS FNL initiated run (Figure 18b) shows some representation of the drier air around 850 hPa, but is too moist at 700 hPa. There is also far less CAPE in this simulated sounding at 669 Jkg^{-1} compared to the observed sounding (approximately 2500 Jkg^{-1}). When the GPS dropwindsondes were assimilated into the WRF on 09 Sept 2006, the sounding corrected towards the GPS dropwindsonde sounding with much drier air showing up below 675 hPa (Figure 18c).

An additional example of the improvement seen using the skew-T plots appears when comparing the first GPS dropwindsonde on 12 Sept 2006 at 25.7^{o}W and 15.6^{o}N (Figure 19a). This GPS dropwindsonde was released around 1300 UTC at approximately 280 hPa and reveals a sounding with SAL between 600 hPa and 900 hPa, which is a bit lower than expected. A comparison sounding was created from the same location in the GFS FNL-initialized simulation without observation nudging at the same time (Fig. 19b) and shows a sounding that is more moist at the mid-levels from 500 hPa to 700 hPa. The presence of the SAL can be identified by the inversion around 975 hPa, with significant warming above this level. This shows that the initialization data was able to capture some presence of the SAL. Figure 19c shows how the assimilated GPS dropwindsonde data was able to correct the atmospheric profile with a more significant inversion at about 950 hPa and much drier conditions extending up to 500 hPa. A significant dry spike is seen in the region that would be identified as the SAL (550 hPa to 675 hPa). There is also a 50 kt ($25ms^{-1}$) wind barb that appears at 650 hPa, coincident with the dry SAL air and is likely a signature of the AEJ. The vertical resolution of the GPS dropwindsondes does outweigh the vertical resolution of

the WRF with the former having hundreds of data points, while the latter has 27 levels between the surface and 100 hPa. These model profiles could be improved with increased resolution.

4. Conclusions

This study is on simulating the AEW environment in association with TC-genesis in the Eastern Atlantic. GPS dropwindsonde data collected during NAMMA 2006 was assimilated into the WRFV3.1.1 to better prescribe the mesoscale environment of AEW 7 south of the Cape Verde Islands. By using the GFS Final Analysis (FNL) dataset in conjunction with the GPS dropwindsondes, this study is aiming to determine the relative role of SAL in the development of hurricanes in this region.

The WRF simulations were able to capture the AEW 7 as it transitioned from a continental airmass to a maritime airmass as well as the formation of tropical depression (pre-Helene). Sensitivity tests were conducted to isolate the most significant variable (temperature, relative humidity, or wind speed) in the GPS dropwindsonde data. AEW 7 eventually became a category 3 hurricane (Helene 2006) over the central North Atlantic after ingesting dry, dusty air from the SAL for a few days.

After assimilating available GPS dropwindsonde data into the WRF simulations of both systems, temperature, RH, and wind analyses were conducted, and it was determined that the temperature plays the most significant role in the simulated intensity of the TC. The difference in pressure between the simulation without GPS dropwindsondes and the simulation with temperature nudging was 15 hPa. There were additional improvements noted in the RH and temperature fields, although the GFS FNL dataset is limited in adequate data coverage in this region of the world to properly capture this complex environment. The assimilated RH introduced moisture and temperature gradients which are more likely to occur in the eastern North Atlantic than the GFS FNL dataset would suggest. The assimilated

GPS dropwindsonde wind appears to have a greater impact on the advection of moisture and temperature into and around the TC circulation. When all three variables (moisture, temperature, and winds) from the GPS dropwindsondes were assimilated, a more representative environment is simulated compared to satellite retrievals and any available in-situ observations. Particularly, the winds can change the storm circulation and eventually change tracks. We plan to further address this area in terms of track and intensity verification is a following study. Additionally, the SLP of the simulated AEW 7 improves by 29 hPa. Skew-T diagrams emphasized the improvements by showing a much better representation of the atmospheric column in the GPS dropwindsonde simulations versus the no GPS dropwindsonde runs. In this study the GPS dropwindsondes provided some improvements in the vertical structure of the environment when compared to model-derived Skew-T diagrams. Apparently, it is necessary to have more vertical levels in the model in order to fully take advantages on GPS dropwindsondes.

Having an accurate synoptic and mesoscale environment simulated will allow for future indepth studies of SAL-TC interactions. Using model initialized datasets with additional observations assimilated leads to better simulation. We can conclude that additional GPS dropwindsondes released in this area of the world may improve model and human forecasts substantially. A separate paper will be presented the intricate details of the SAL interaction with TCs in terms of tracks and intensity.

Acknowledgments

The critical reviews of anonymous reviewers and the editor were very helpful. We acknowledge the suppliers of datasets utilized in this research. We wish to express our appreciation to T. Eichler and G. Chen for the suggestions for the development of this research. This research was partly supported by the National Science Foundation Grant AGS-1209296.

References

Braun S (2010) Reevaluating the role of the saharan air layer in atlantic tropical cyclogenesis and evolution. Mon. Wea. Rev., 138, 2007 - 2037.

Burpee R (1972) The origin and structure of easterly waves in the lower troposphere in North Africa. J. Atmos. Sci., 29, 77 - 90.

Carlson T, Prospero J (1972) The large-scale movement of saharan air outbreaks over the northern equatorial atlantic. J. Appl. Meteor., 11, 283-297.

Centeno D, Chiao S (2015) The Footprints of Saharan Air Layer and Lightning on the Formation of Tropical Depressions over the Eastern Atlantic Ocean, Meteorology and Atmospheric Physics, 127, 17-32.

Chen YL (1985) Tropical squall lines over the eastern Atlantic during GATE. Mon. Wea. Rev., 113, 2015-2022.

Chou MD, Suarez MJ (1994) An efficient thermal infrared radiation parameterization for use in general circulation models, NASA Tech. Memo. 104606, vol. 3, pp. 85, 1994.

Diaz H, Carlson T, Prospero J (1976) A study of the structure and dynamics of the Saharan air layer over the northern equatorial atlantic during BOMEX. Tech. Rep. ERL WMPO-32, National Hurricane and Experimental Meteorology Laboratory, NOAA, 61 pp

Dunion J (2011) Re-writing the climatology of the tropical north atlantic and caribbean sea atmosphere. J. Climate, 24 no. 3, 893-908.

Dunion J, Velden C (2004) The impact of the Saharan air layer on Atlantic tropical cyclone activity. Bull. Amer. Meteor. Soc., 85, 353-365.

Emanuel K (1989) The finite-amplitude nature of tropical cyclogenesis. J. Atmos. Sci., 46, 3431-3456.

Folmer M (2009) Validation of the WRF forecasts of the development of Hurricane Helene 2006. M.S. thesis, Saint Louis University, 124 pp.

Hock TF, Franklin JL (1999) The NCAR GPS Dropwindsonde. Bulletin of the American

Meteorological Society, 80, 407-420.

Hong SY, Noh Y, Dudhia J (2006) A new vertical diffusion package with an explicit treatment of entrainment processes. Mon. Wea. Rev., 134, 2318-2341.

Janjic ZI (2001) Nonsingular Implementation of the Mellor-Yamada Level 2.5 scheme in the NCEP meso model. National Centers for Environmental Prediction, Office Note #437.

Powell M (1990) Boundary layer structure and dynamics in outer hurricane rainbands. part II: Downdraft modification and mixed-layer recovery. Mon. Wea. Rev., 118, 918-938.

Mlawer EJ, Taubman SJ, Brown PD, Iacono MJ (1997) Radiative transfer for inhomogeneous atmospheres: RRTM, a validated correlated-k model for the longwave. J. Geophys. Res. Vol. 102, 16663-16682.

Schwendike J, Jones S (2010) Convection in an African EasterlyWave overWest Africa and the eastern Atlantic. a model case study of Helene (2006). Quart. J. Royal Meteor. 436 Soc., 136, 364-396.

Sun D, Lau W, Kafatos M, Boybeyi Z, Leptoukh G, Yang C, Yang R (2009) Numerical simulations of the impacts of the Saharan air layer on Atlantic tropical cyclone development. J. Climate, 22, 6230-6250.

Tuleya RE, Lord SJ (1997) The Impact of Dropwindsonde Data on GFDL Hurricane Model Forecasts Using Global Analyses. Wea. Forecasting, 12, 307-323.

Wang J, and coauthors (2015) A Long-Term, High-Quality, High-Vertical-Resolution GPS Dropsonde Dataset for Hurricane and Other Studies. Bull. Amer. Meteor. Soc., 96, 961973.

Wu C, Chou K, Lin P, Aberson S, Peng MS, Nakazawa T (2007) The impact of dropwindsonde data on typhoon track forecasts in DOTSTAR. Wea. Forecasting, 22, 1157-1176.

Zawislak J, Zipser E (2010) Observations of seven African easterly waves in the East Atlantic during 2006. J. Atmos. Sci., 67, 26-43.

Zipser E et al (2009) The Saharan air layer and the fate of African easterly waves: NASA's AMMA 2006 field program to study tropical cyclogenesis. Bull. Amer. Meteor. Sci., 90, 1137-1156.

List of Tables

Table 1. Sensitivity experiments.

Cases	*Assimilation Component*
wGPS	only wind component from dropsondes
nGPS	no GPS dropsondes assimilated
tGPS	only temperature component from dropsondes
rGPS	only RH component from dropsondes
aGPS	all three components from dropsondes

List of Figures

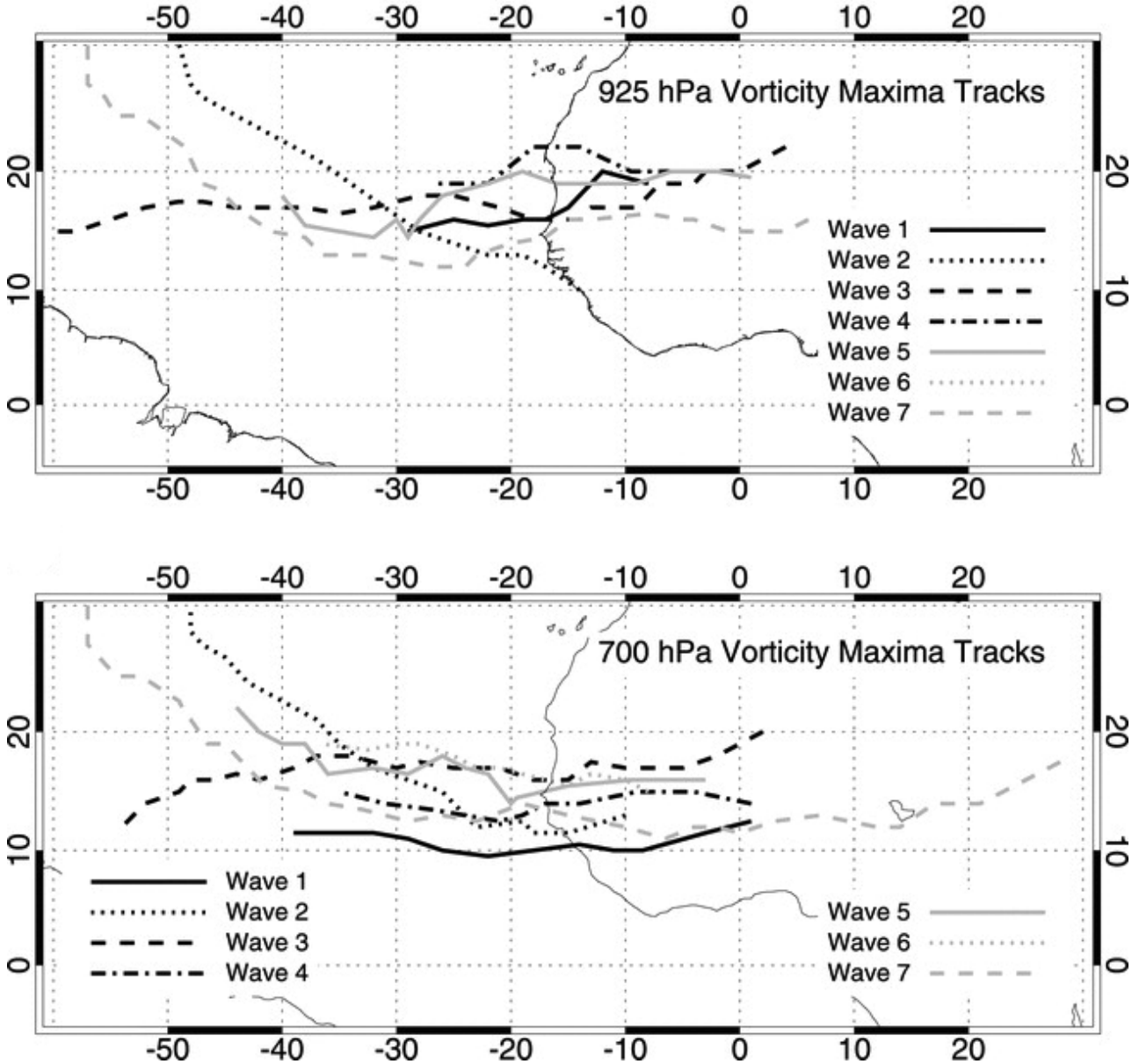

FIG. 1. The Global Data Assimilation System (GDAS) analyzed (a) 925- and (b) 700-hPa vorticity maxima tracks for the seven AEWs of NAMMA (Zawislak and Zipser 2010, p. 29)

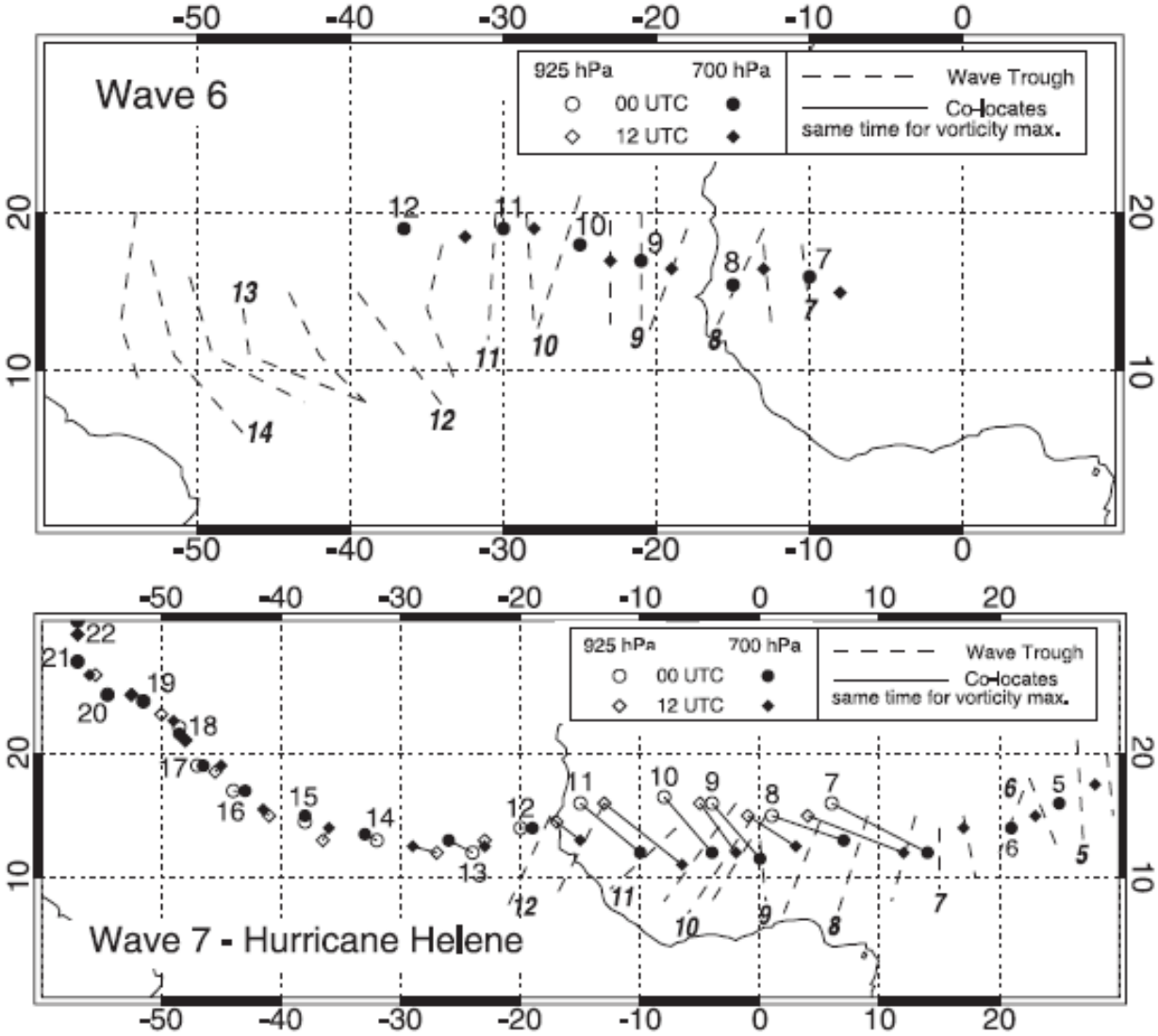

Fig. 2. GDAS-analyzed 925- and 700-hPa vorticity maxima and 700-hPa wave trough locations for (a) wave 6 at 0000 and 1200 UTC, and (b) wave 7 at 0000 and 1200 UTC. Numbers indicate the day of the month (at 0000 UTC) for the vorticity maxima (nonitalic) and for the 700-hPa wave trough (italic).(Zawislak and Zipser 2010, p. 39)

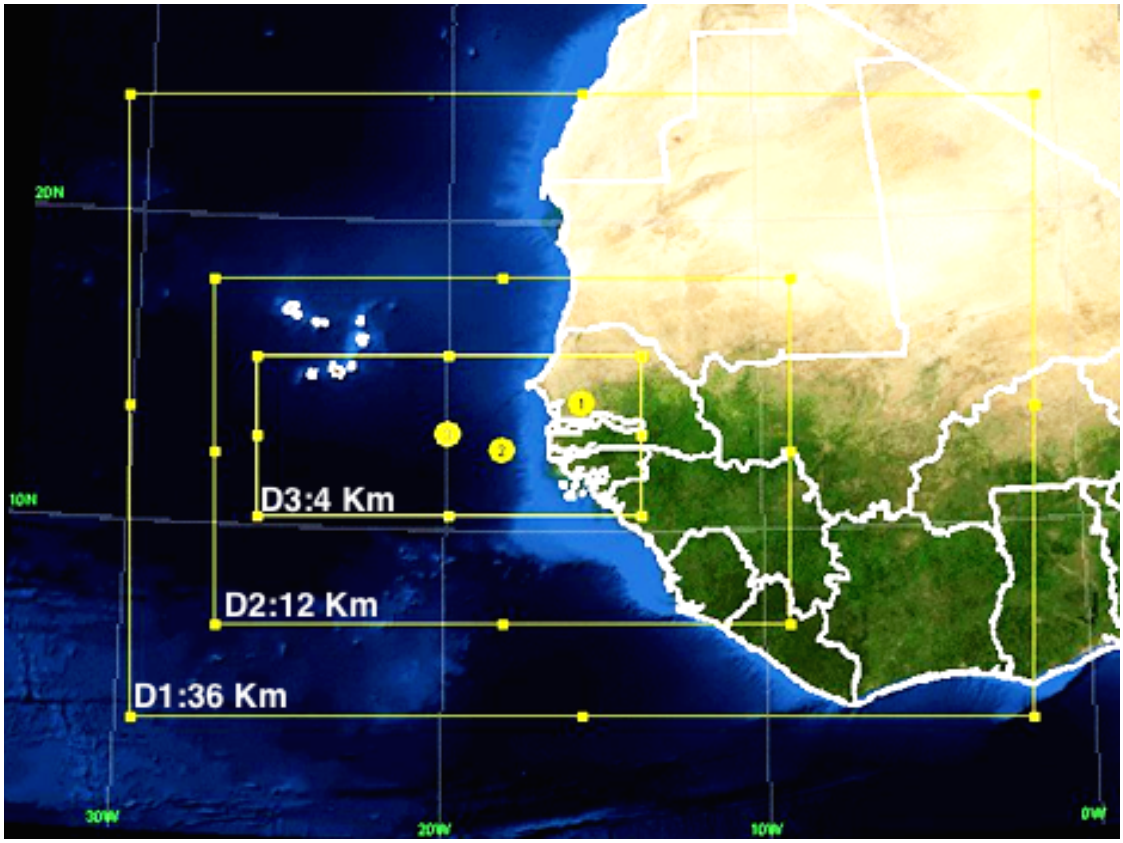

FIG. 3. The domains used for the WRF study of the evolution of wave 6 and wave 7 (Helene) in 2006.

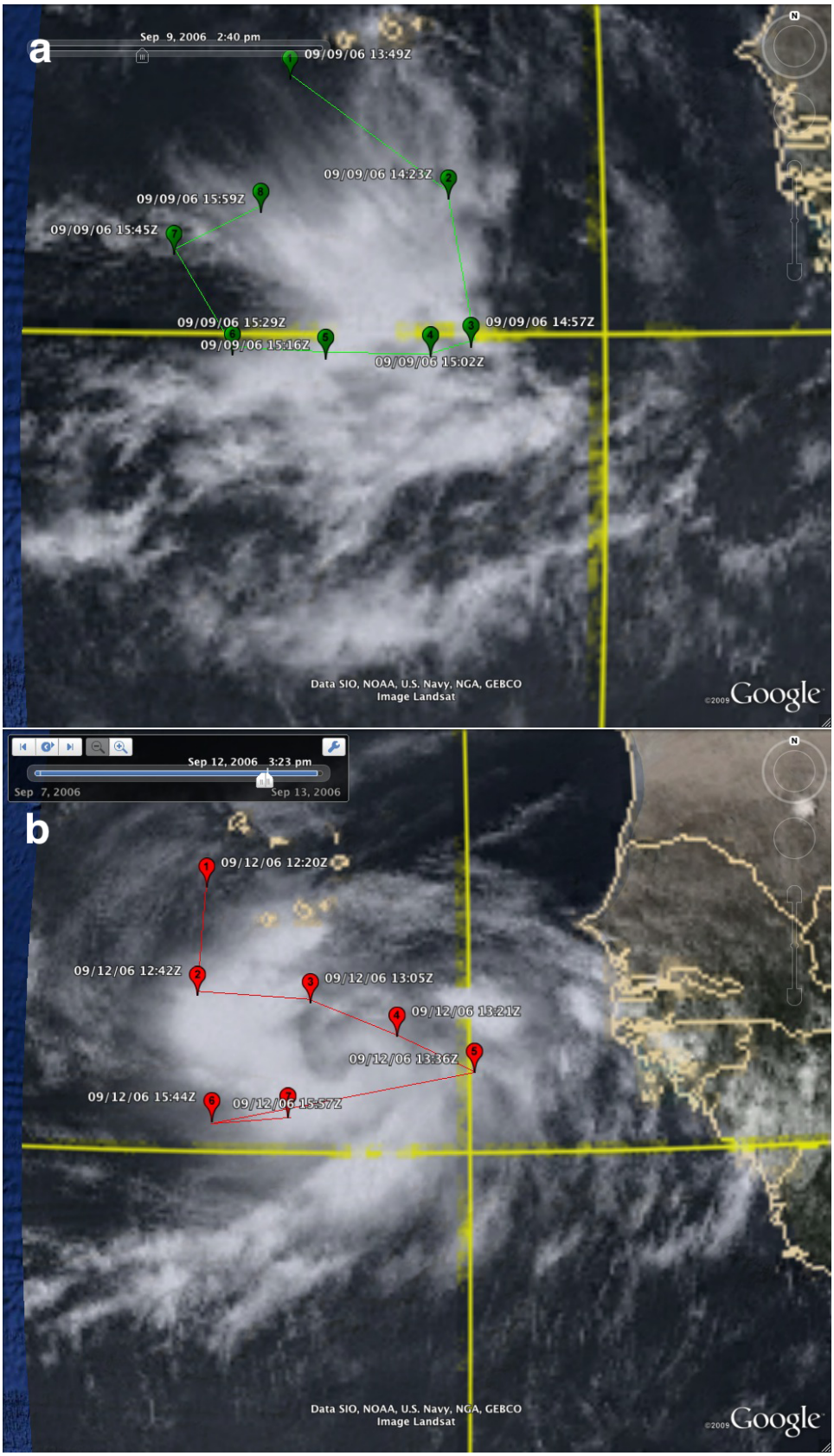

FIG. 4. The locations of the dropsonde with overlaid MODIS satellite imagery for (a) sondes dropped on September 9, and (b) sondes dropped on September 12, 2006.

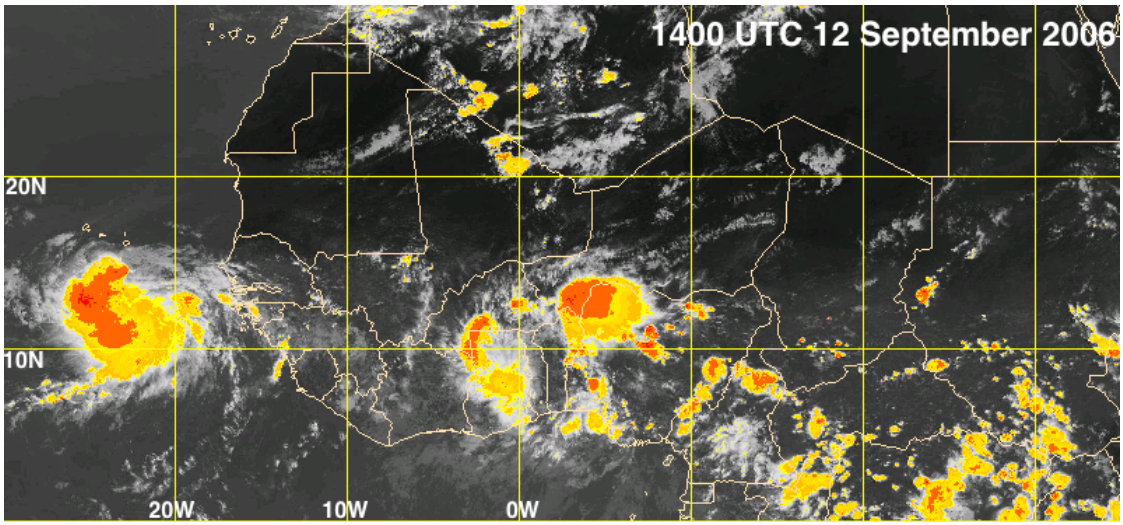

FIG. 5. Meteosat 8 infrared images (10.8 μm channel) where convective objects are superimposed using shadings of grey above -64°C, orange-red colours between -64° and -82°C and black below -82°C.

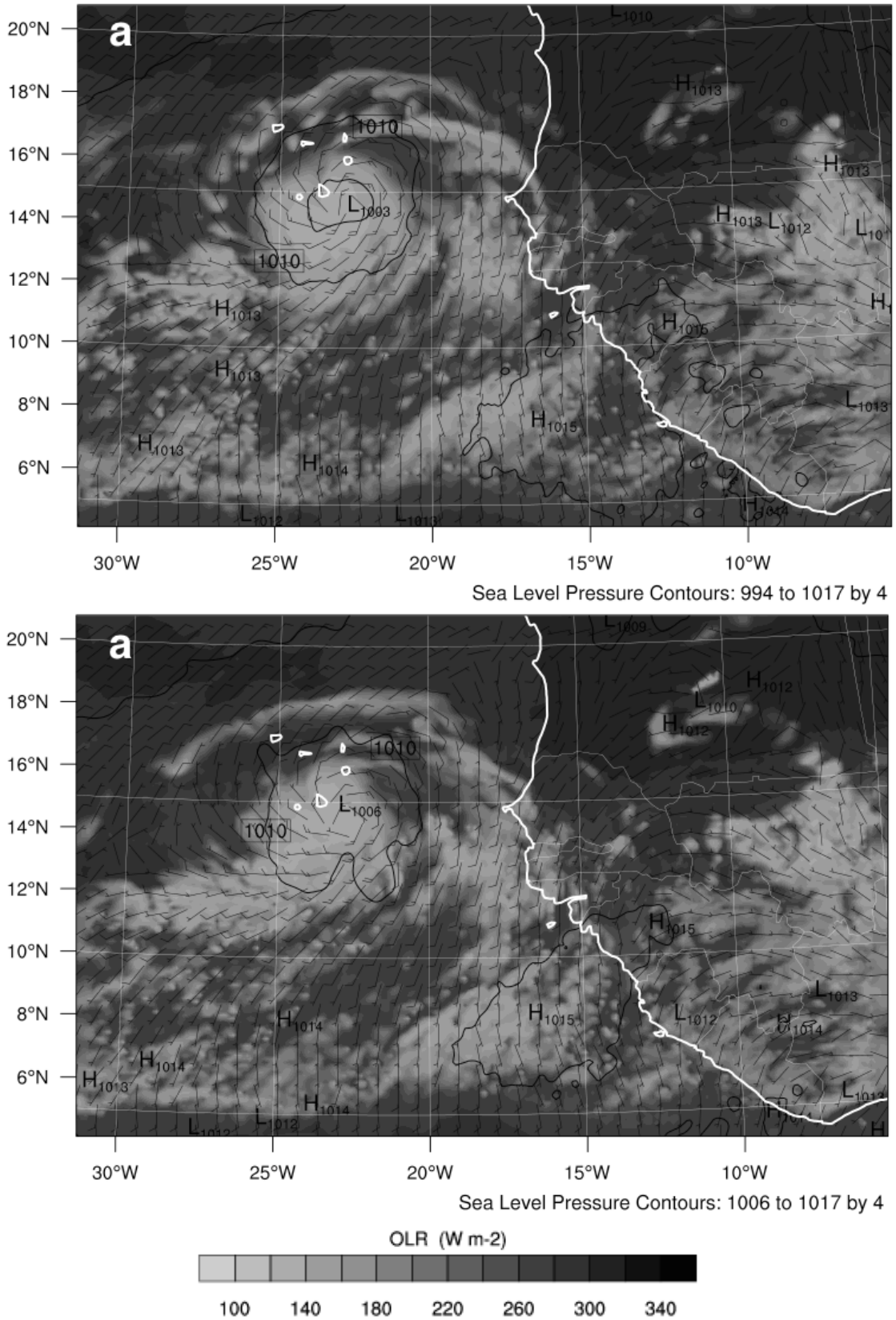

FIG. 6. OLR imagery from the WRF simulation (a) without GPS dropsondes, and (b) with GPS dropsondes valid at 1400 UTC on 12 Sept 2006.

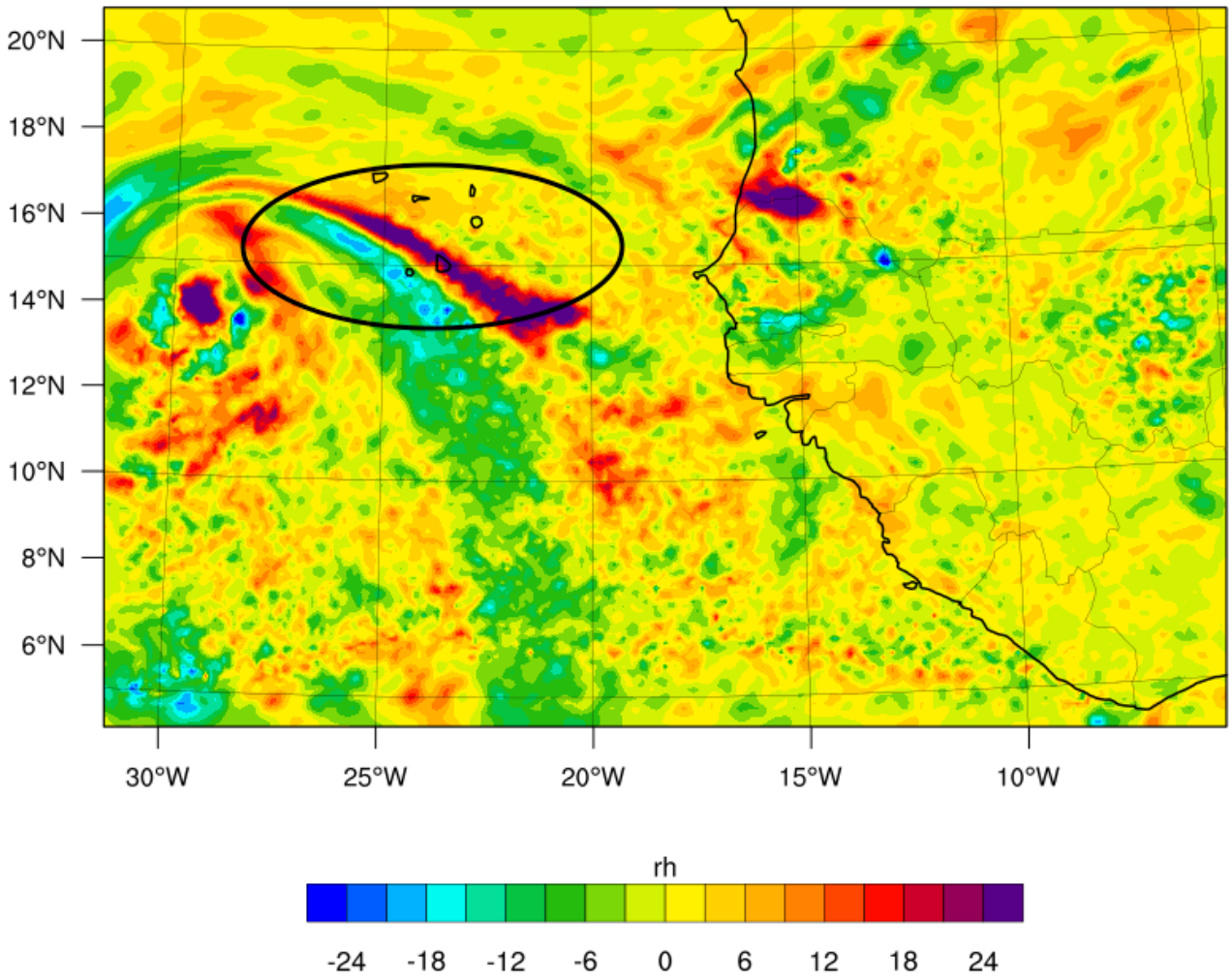

FIG. 7. The difference in RH values at 600 hPa when subtracting simulation wGPS from simulation nGPS valid at 1200 UTC 13 Sept 2006. Units are in %. The black ellipse highlights a band of higher RH values in simulation nGPS that is not present in simulation wGPS.

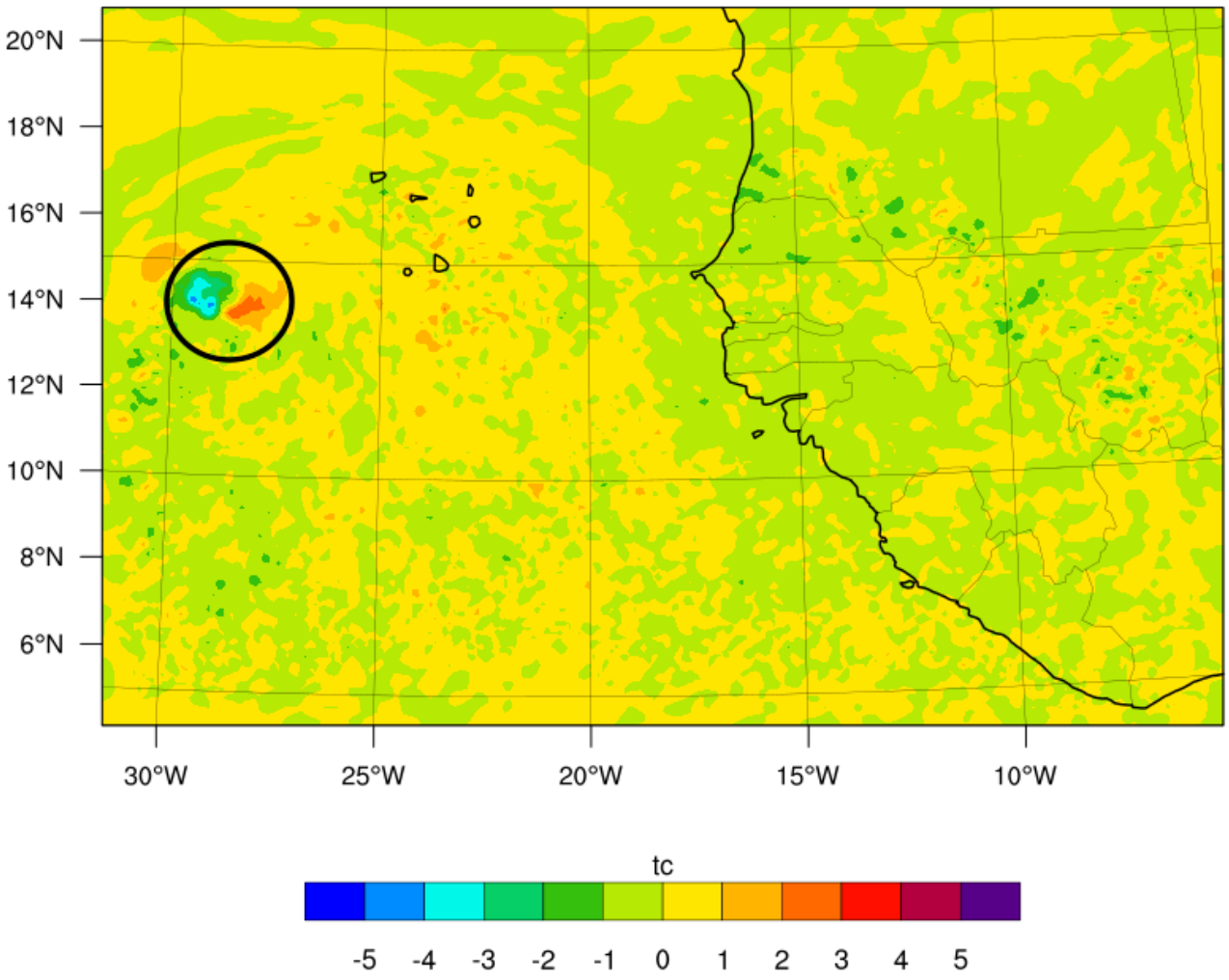

FIG. 8. The difference in temperature at 700 hPa by subtracting simulation wGPS from simulation nGPS valid at 1200 UTC 13 Sept 2006. Units are in ^{o}C. The black circle highlights the temperature differrence near the TC center.

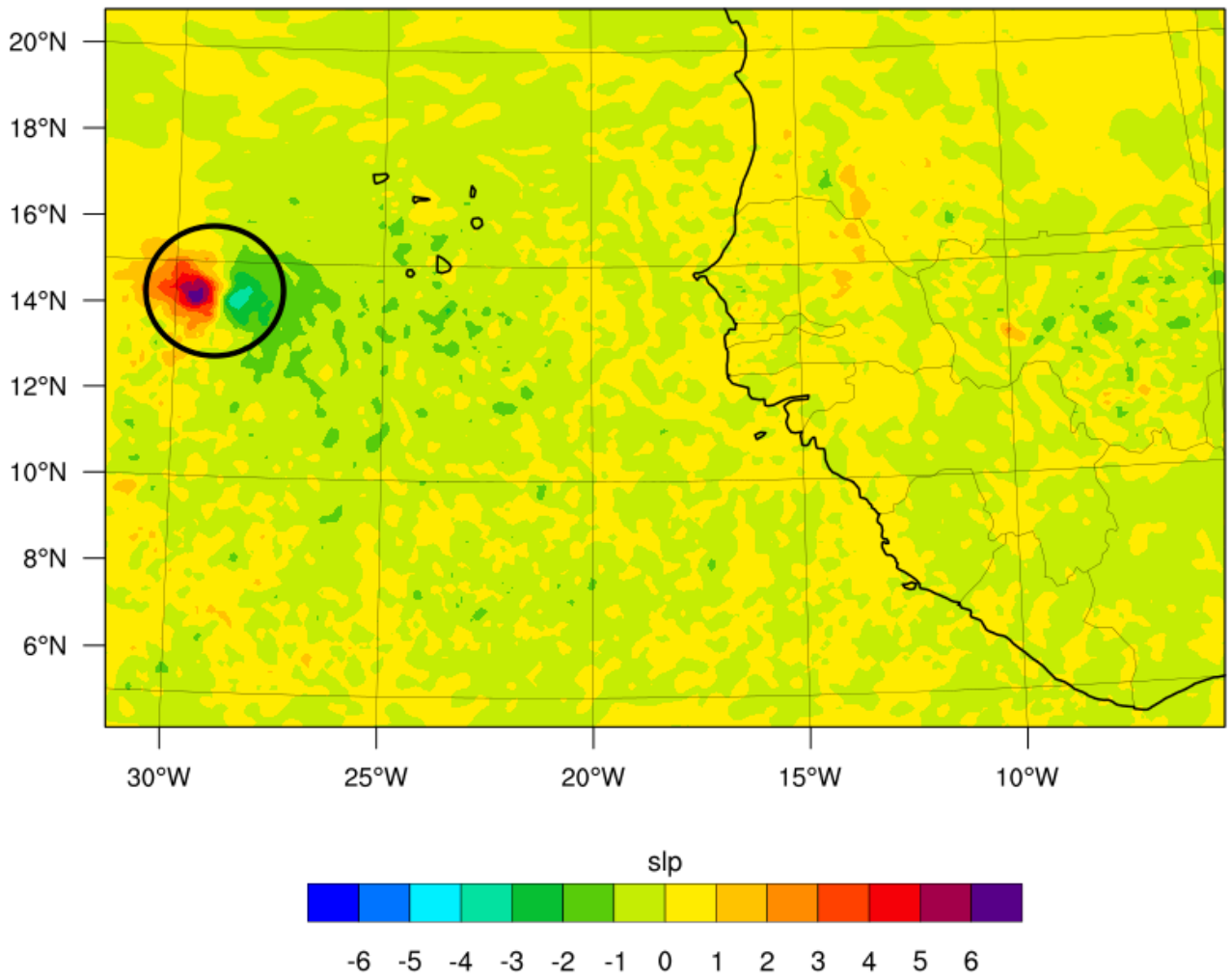

FIG. 9. The difference in sea level pressure by subtracting simulation wGPS from simulation nGPS valid at 1200 UTC 13 Sept 2006. Units are in hPa. The black circle highlights the pressure difference near the TC center.

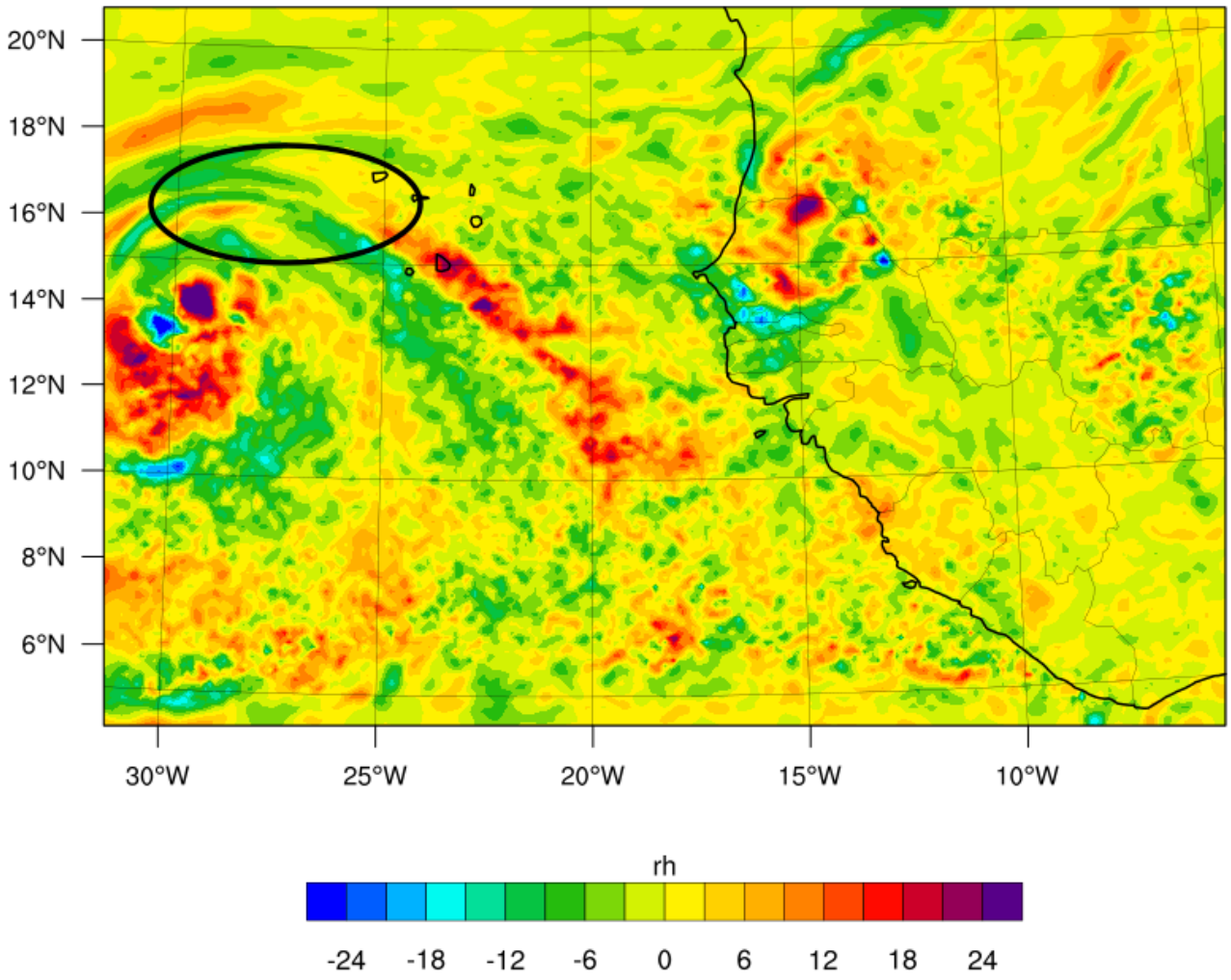

FIG. 10. The difference in RH values at 600 hPa by subtracting simulation tGPS from simulation nGPS valid at 1200 UTC 13 Sept 2006. Units are in %. The black ellipse highlights a band of higher RH values in simulation nGPS that is not present in simulation tGPS.

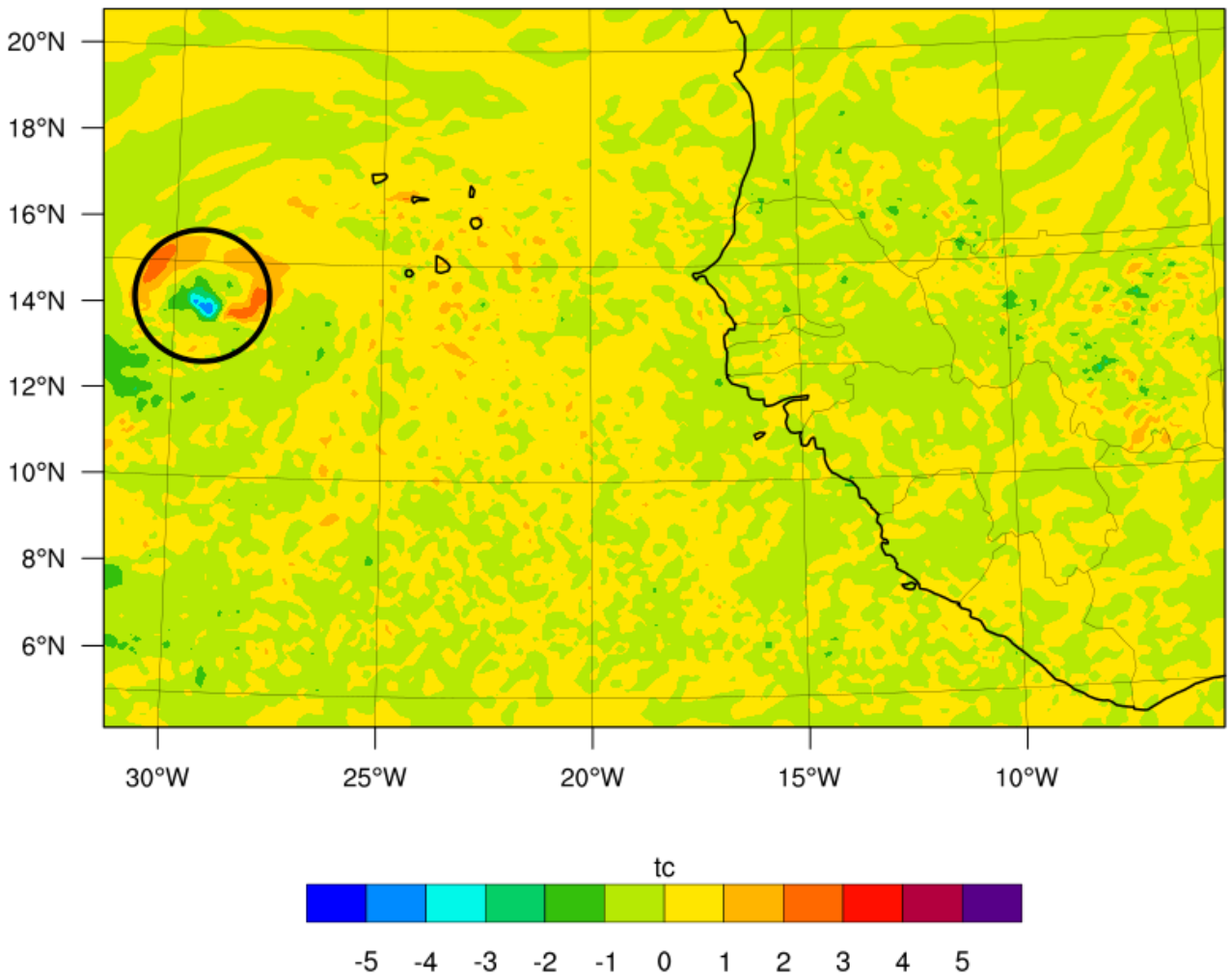

FIG. 11. The difference in temperature at 700 hPa by subtracting simulation tGPS from simulation nGPS valid at 1200 UTC 13 Sept 2006. Units are in ^{o}C. The black circle highlights the temperature difference near the TC center.

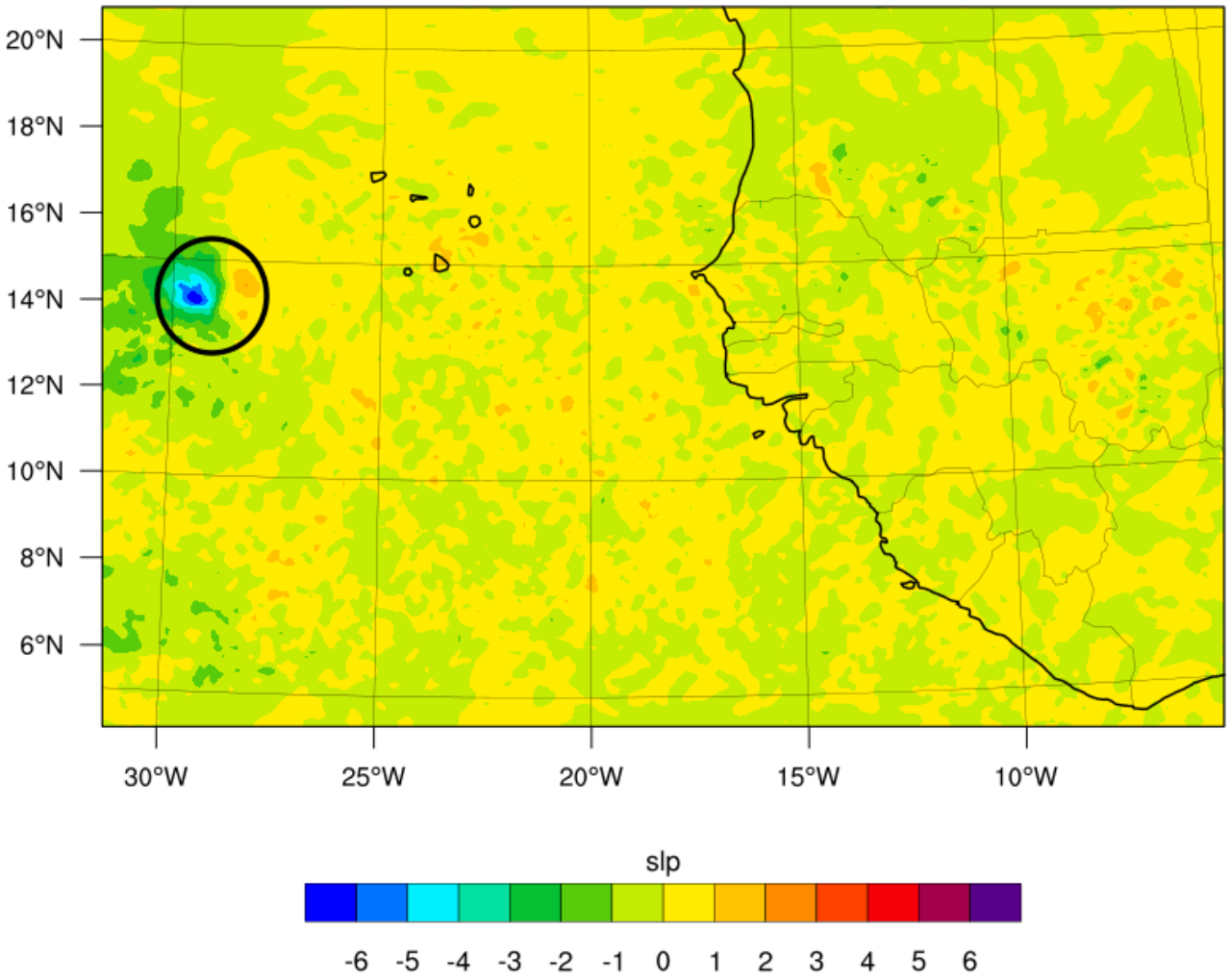

FIG. 12. The difference in sea level pressure by subtracting simulation tGPS from simulation nGPS valid at 1200 UTC 13 Sept 2006. Units are in hPa. The black circle highlights the pressure difference near the TC center.

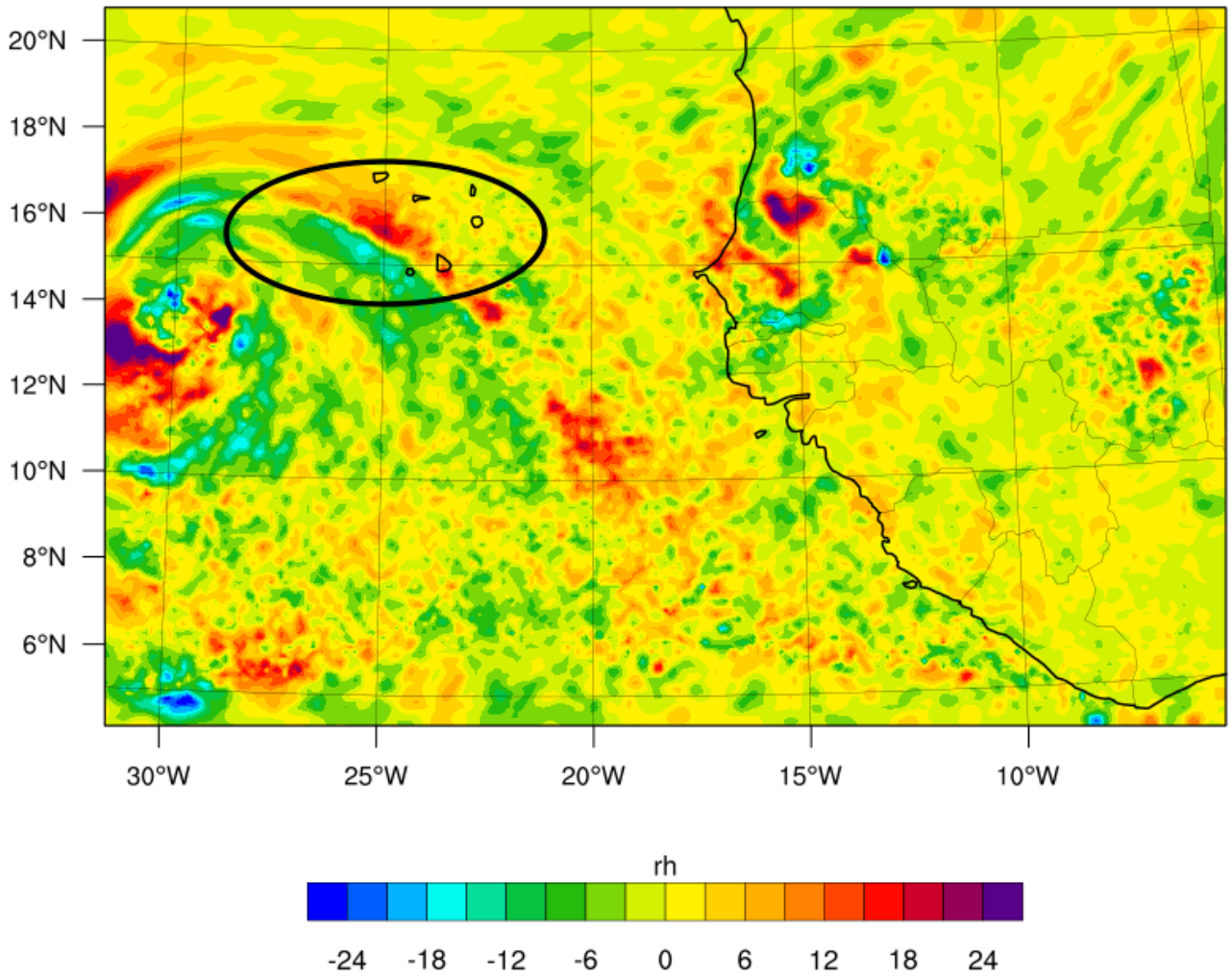

FIG. 13. The difference in RH values at 600 hPa by subtracting simulation rGPS from simulation nGPS valid at 1200 UTC 13 Sept 2006. Units are in %. The black ellipse highlights a band of higher RH values in simulation nGPS that is not present in simulation rGPS.

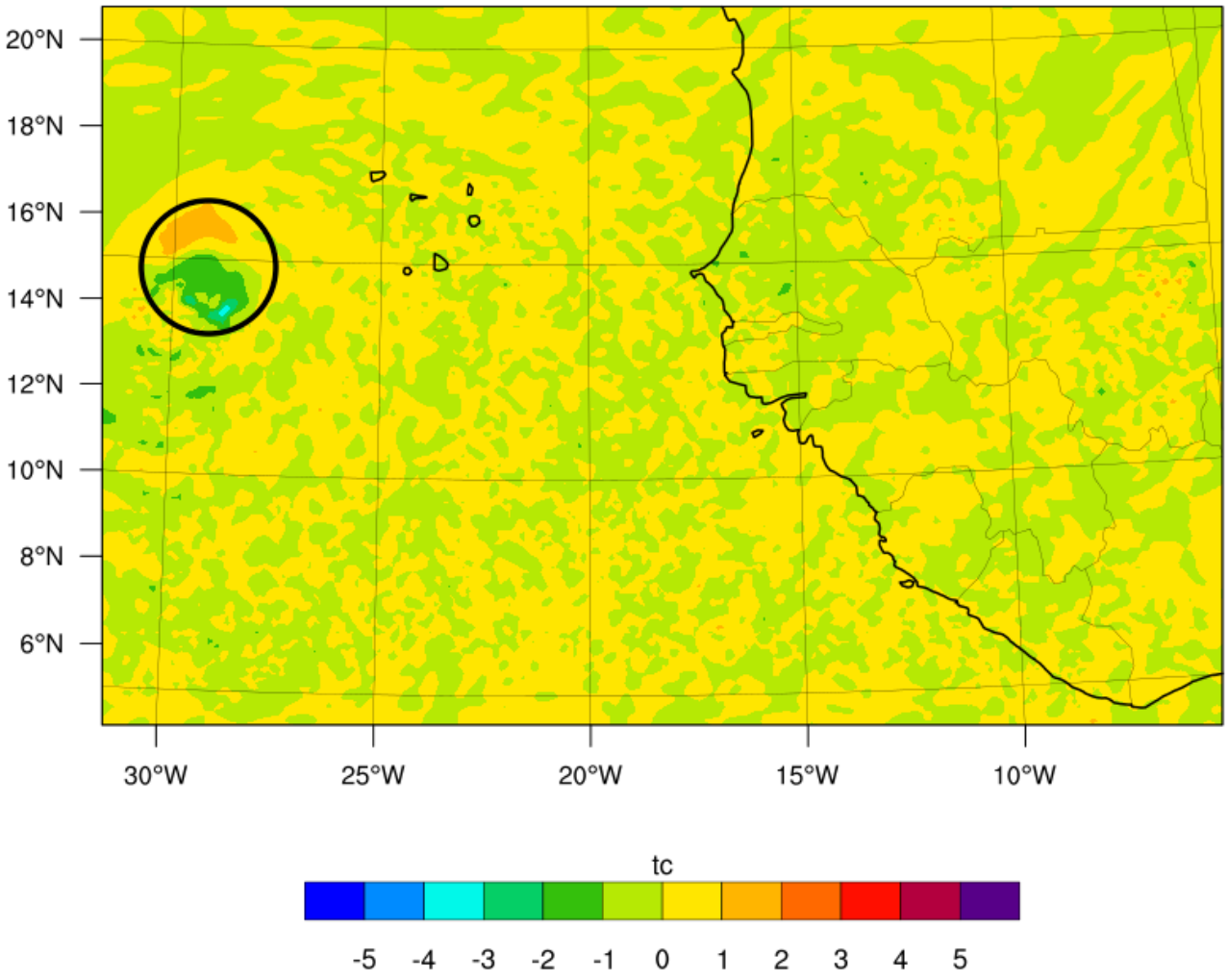

FIG. 14. The difference in temperature at 700 hPa by subtracting simulation rGPS from simulation nGPS valid at 1200 UTC 13 Sept 2006. Units are in ^{o}C. The black circle highlights the temperature difference near the TC center.

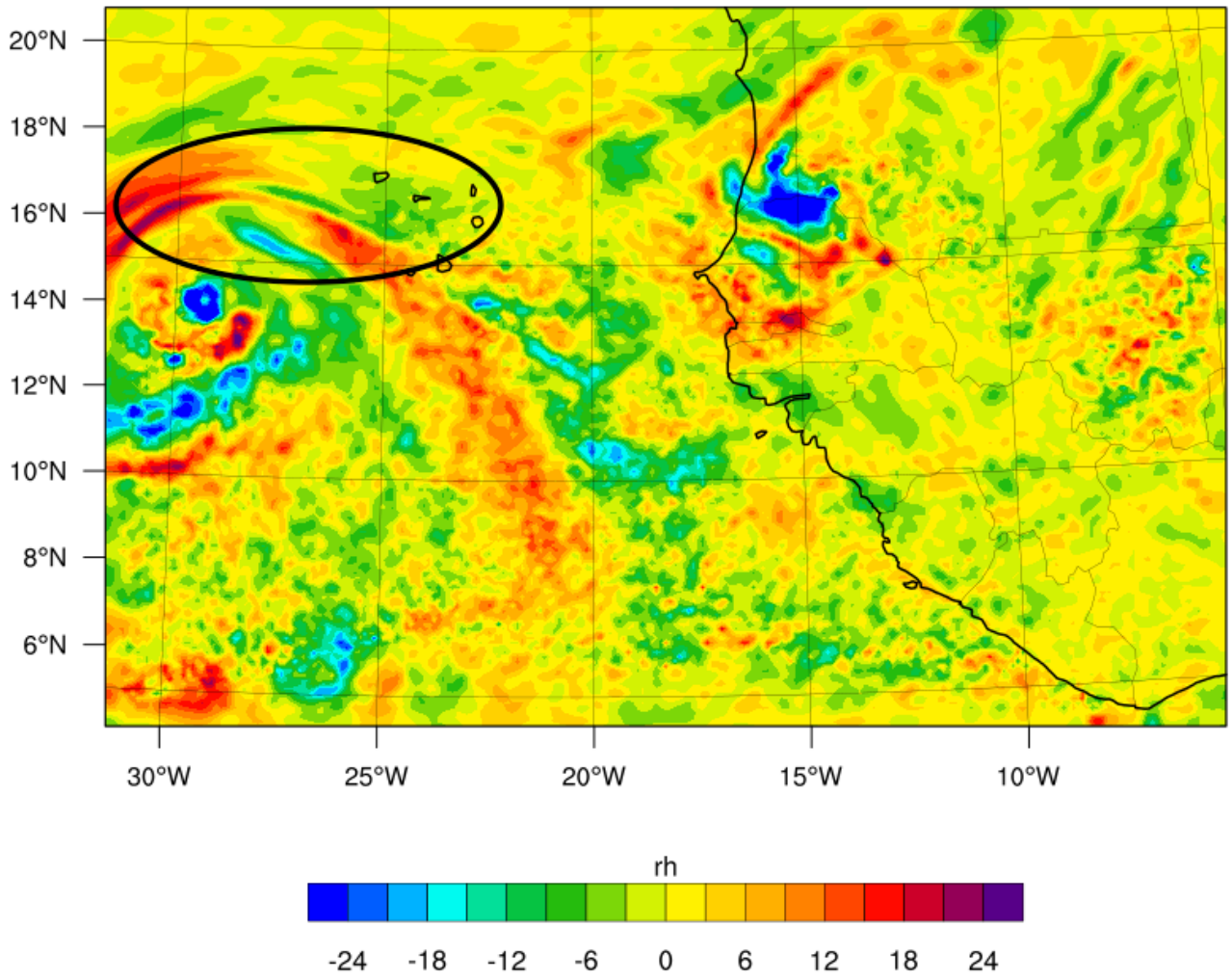

FIG. 15. The difference in RH values at 600 hPa by subtracting simulation aGPS from simulation nGPS valid at 1200 UTC 13 Sept 2006. Units are in %. The black ellipse highlights a band of higher RH values in simulation nGPS that is not present in simulation aGPS.

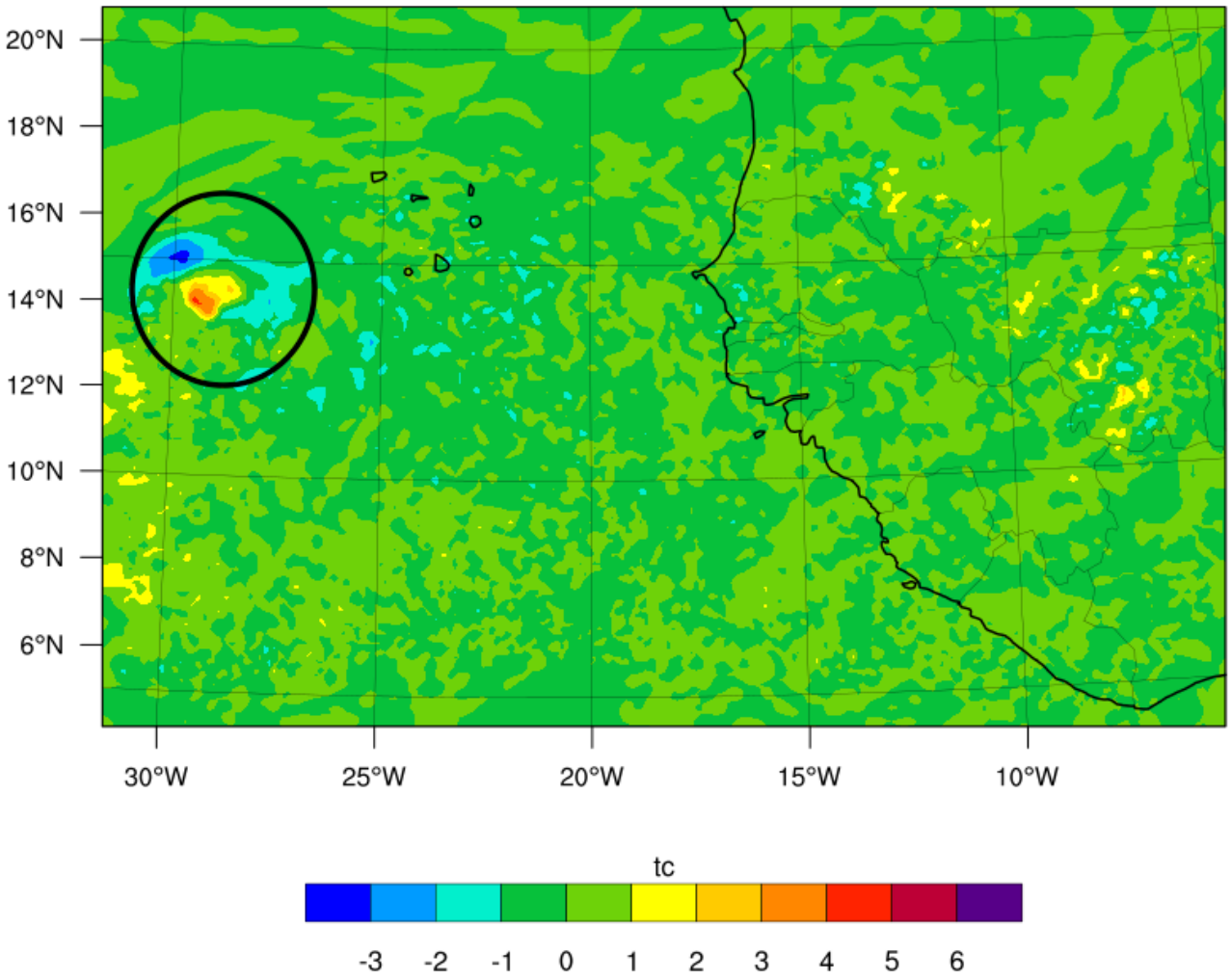

FIG. 16. The difference in temperature at 700 hPa by subtracting simulation aGPS from simulation nGPS valid at 1200 UTC 13 Sept 2006. Units are in ^{o}C. The circle highlights the temperature difference near the TC center.

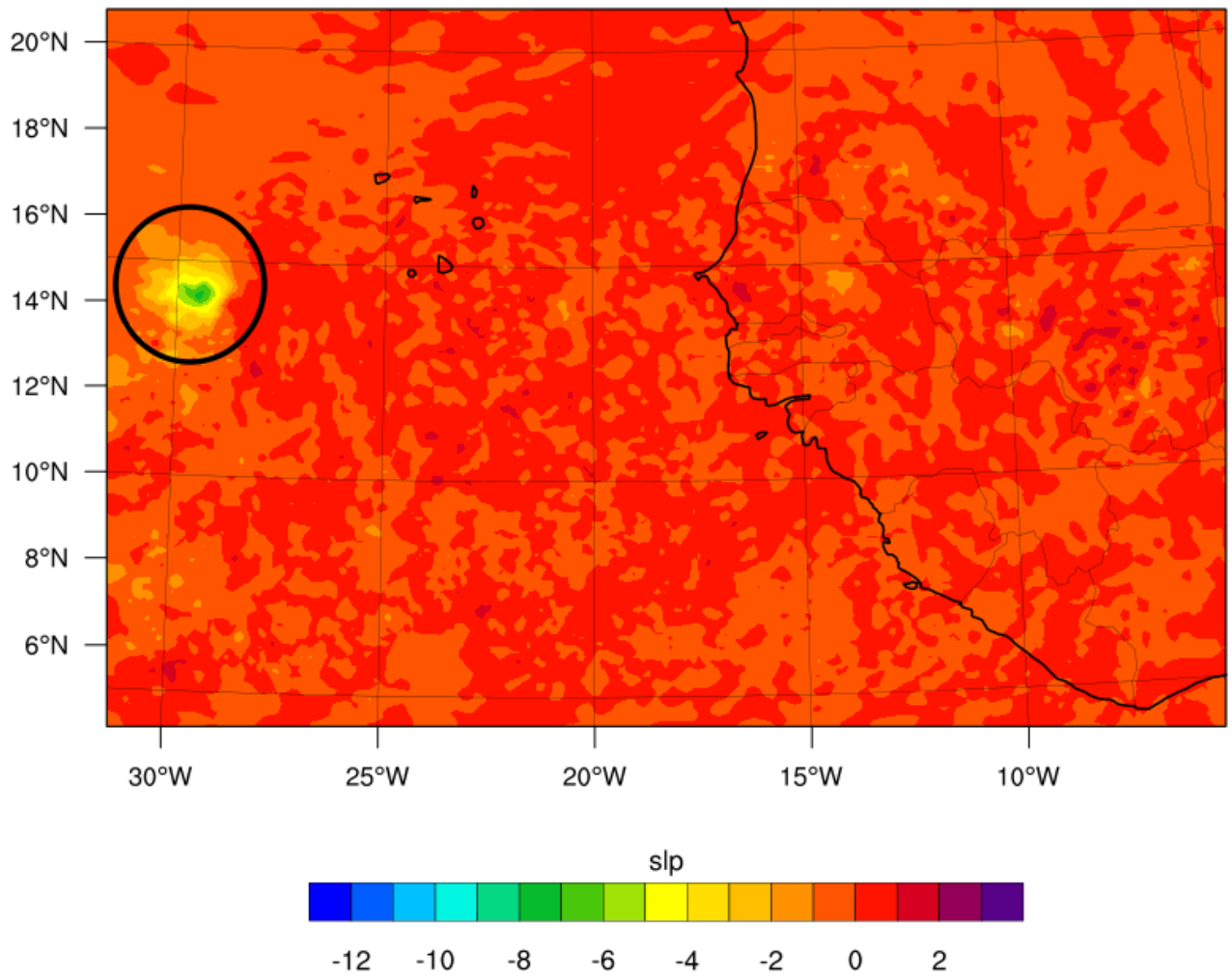

FIG. 17. The difference in sea level pressure by subtracting simulation aGPS from simulation nGPS valid at 1200 UTC 13 Sept 2006. Units are in hPa. The black circle highlights the pressure difference near the TC center.

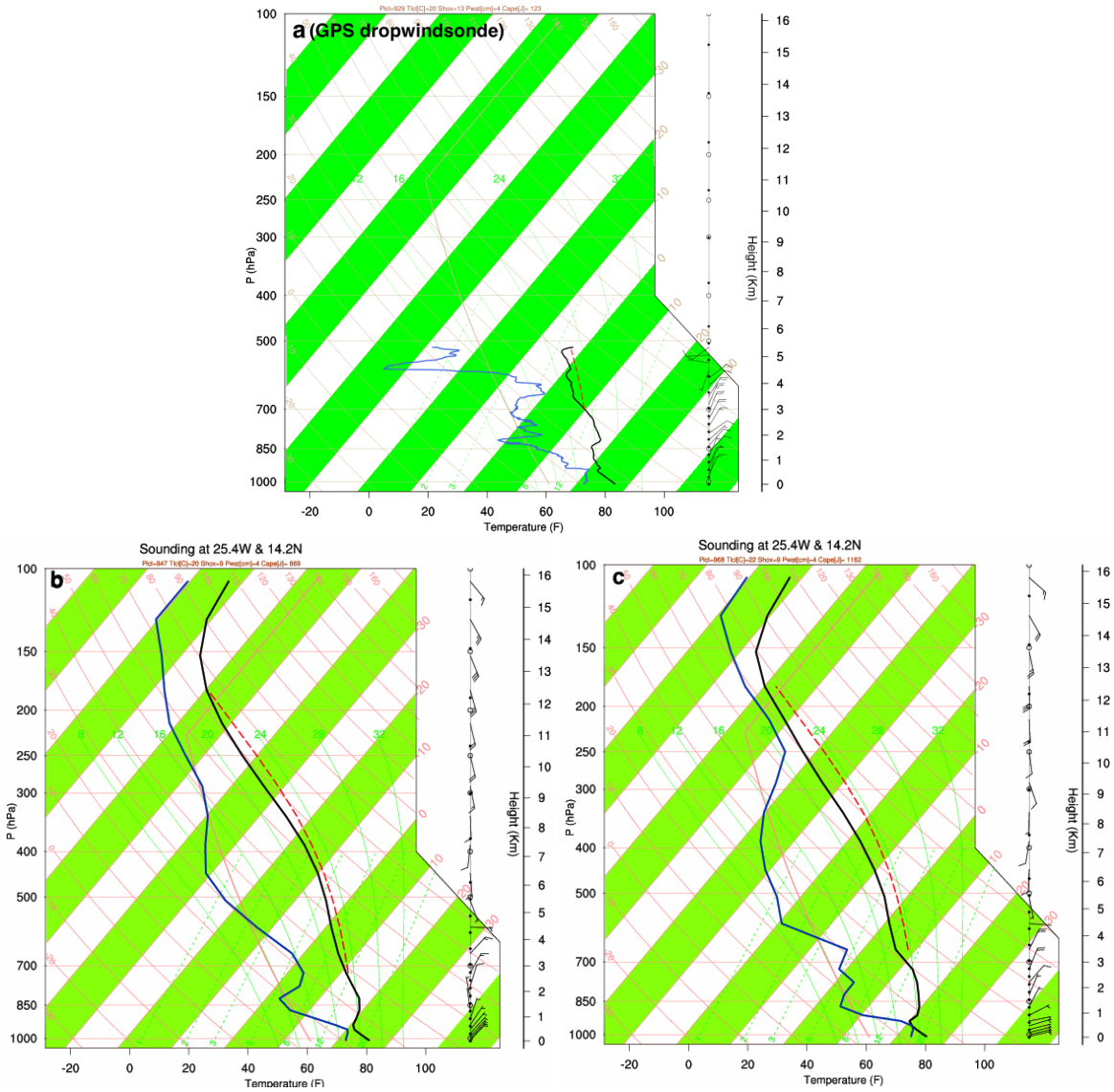

FIG. 18. Skew-T plot from the (a) GPS dropsonde, (b) without GPS dropsondes, and (c) with GPS dropsondes valid at 1400 UTC on 09 Sept 2006 at 25.4^{o}W and 14.2^{o}N.

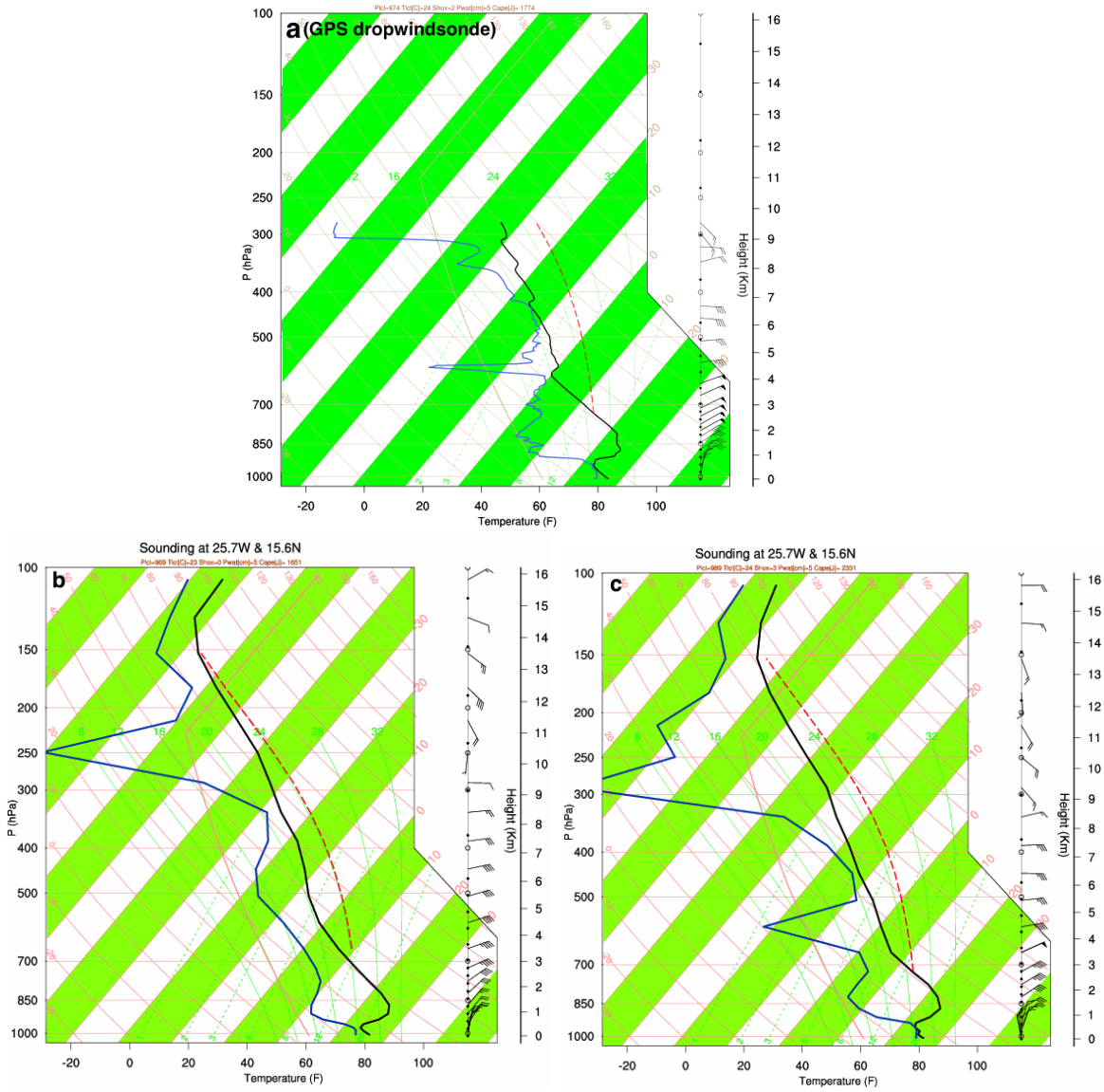

FIG. 19. Skew-T plot from the (a) GPS dropsonde, (b) simulation without GPS dropsondes, and (c) simulation with GPS dropsondes valid at at 1300 UTC on 12 Sept 2006 at 25.7^{o}W and 15.6^{o}N.